

Chemical compatibility of hollow ceramic cenospheres as thermal insulation for high-temperature thermal energy storage applications with molten nitrate salt

Authors: Youyang Zhao^{1,*}, Emma Wagstaff¹, Samuel Gage^{1,2}, Deanna Payne¹, Craig Turchi¹

¹ National Renewable Energy Laboratory, 15013 Denver West Parkway, Golden, CO 80401, USA

² Energetics, 7075 Samuel Morse Drive, Suite 100, Columbia, MD 21046, USA

*Corresponding author: Youyang.zhao@nrel.gov

Keywords: cenospheres; thermal insulation; chemical compatibility; thermal energy storage; molten nitrate

Abstract

An effective insulation material that is both thermally and chemically stable in molten salts could transform the design of molten-salt-based thermal energy storage (TES) tanks. Most current molten salt TES tanks hold the metallic tank structure in direct contact with hot salt inventory, a design which leads to thermal expansion of the tank and triggers stresses that can lead to thermomechanical failures. With an internal insulation to lower the temperature at the tank structure, the extent of thermal expansion can be reduced, thereby reducing expansion-induced stresses and allowing for consideration of lower-cost tank structure materials.

Conventional insulation materials are either 1) too porous and allow molten salts to permeate into the matrix, which significantly increases the thermal conductivity or 2) too dense and have a thermal conductivity that cannot provide sufficient thermal insulation. This paper presents an alternative thermal insulation concept using cenospheres which have an alumino-silicate structure. The cost analysis suggests that the low-density cenospheres can be one of the cheapest materials to provide cost-effective thermal insulation. The chemical compatibility of cenospheres is investigated in molten 60 wt.% NaNO₃/40 wt.% KNO₃ salt which is close to industrial-grade Solar Salt. This paper shows that diffusion of the sodium and potassium cations from the salt into the cenospheres occurs based on weight analysis, energy dispersive spectroscopy (EDS), X-ray diffraction (XRD) and Fourier-transform infrared (FTIR) spectroscopy. The cation diffusion breaks the bridging oxygen bonds and causes volume expansion of the microstructure which is responsible for the failure of the cenosphere particles. The chemical composition of the cenospheres is found to affect their compatibility with molten nitrate salt. A cenosphere product with low iron content showed the best compatibility with an average survival rate of 77.9% ± 9.8% after 7 days of immersion in the molten nitrate salt. While even low-iron cenospheres appear to require protection from direct molten salt contact, their slow degradation rate, closed-cell porosity, and low cost hold potential for effective use as internal tank insulation.

1. Introduction

Thermal insulation materials are essential for various industrial applications. Different forms of insulation are used for different purposes. For example, highly porous ceramic-based firebricks are used as primary insulation to reduce the temperature of a furnace. Dense firebricks are used to directly interface with a harsh high-temperature and corrosive environment. Other non-fire-brick materials like aerogels were invented for more extreme cases such as aerospace applications.

This paper presents a new insulation concept for a different category of thermal insulation application: long-term storage of high-temperature liquids at above 500°C. This is of particular interest to concentrating solar power (CSP) industry that uses high-temperature fluids such as molten salts to move and store thermal energy for electricity generation. Current molten salt storage in CSP systems uses unlined tanks made of carbon or stainless steel, depending on the salt temperature. Some of these tanks, especially those holding salt at temperatures greater than 400°C, have experienced failures [1]. Internal insulation could address the current thermal energy storage (TES) tank design challenges where excessive thermal expansion of the tank structure due to high operating temperature creates significant mechanical stresses. Reducing the temperature of the tank structure could fundamentally reduce such risks and allow a more reliable TES and improve the competitiveness of CSP [2]. In addition, a lower tank temperature allows a cheaper tank structure material (e.g., switching from stainless steels to carbon steels) which could, in turn, justify the added cost of the internal insulation. More broadly speaking, TES with hot liquids is attracting increasing attention as a key step to allow storage of renewable electricity with a Carnot battery [3], [4].

The universal strategy for creating superior thermal insulation materials is to create gas pockets because stagnant gases usually have a thermal conductivity 1-3 orders of magnitude lower than that of liquids and solids. This strategy has been applied to almost all insulation materials (e.g., fiberglass batts [5]–[7], porous refractory bricks [8]–[15], aerogels and foams [16]–[21], etc.). However, most of these materials have open and inter-connected porosities that are less useful when insulating liquids. When these porosities are wetted by the liquids, the gas pockets (air pockets in most cases) will be displaced and the material will lose thermal insulation capability. A nonpermeable, protective layer or membrane can be used to avoid insulation wetting, but such features increase cost, complexity, and risk of a small leak quickly destroying the insulation. Therefore, the preferred requirements for insulating liquids are 1) to have enclosed rather than open porosities and 2) to have independent rather than inter-connected porosities. The former is to retain insulation capability when in contact with the liquids whereas the latter is to reduce the risk of overall insulation failure when one pore is wetted allowing the liquid to propagate to other pores through their interconnectivity.

For high-temperature molten salts, the materials of interest in this paper are oxide-based hollow ceramic microspheres with diameters around 1-300 μm such as alumino-silicate-based cenospheres. These materials and other oxide-based hollow spheres have been a research interest because of their low bulk density and low thermal conductivity [22]–[26]. Most of the applications involve placing the hollow spheres as inclusions inside a matrix to improve its thermal insulation, enhance mechanical strength, and/or reduce density. For example, the hollow spheres are mixed into aerogels [27]–[29], concrete [30]–[36], coatings and thin films [37]–[43], fibers/textiles [44]–[48], foams [49]–[58] and polymers [59]–[69], and other miscellaneous materials [70], [71]. There are also attempts to sinter the free-flowing hollow spheres to form a self-supporting structure [72]–[75]. While hollow ceramic microspheres have been widely studied as an insulation material, to our best knowledge the direct use of hollow oxide-spheres as insulation without a matrix has not been extensively explored. Cenospheres show promise as a high-temperature insulation material for corrosive environments for the following reasons:

1. Cenospheres themselves have excellent thermal insulation.
2. Cenospheres can be more chemically resistant and mechanically stronger than some matrix materials such as aerogels. Motte et al. [76] performed corrosion tests in molten 60 wt.% NaNO₃/40 wt.% KNO₃ salt of a ceramic block made by re-melting fly ash particles – which have very similar chemistry to cenospheres – and showed that the fly ash chemistry is stable after 500 hours at 500°C.
3. The TES operating temperature is up to 565°C for current generation CSP¹ and cenospheres are thermally stable in air at these temperatures.
4. Most importantly, cenospheres are inexpensive which is crucial in a cost-sensitive large-scale application such as TES with molten salt.²

By first-order approximation, materials insulate by volume instead of by mass. Therefore, an insulation material with low density can have a cost advantage over an insulation material with higher density. For example, a reference conventional porous fire brick material that is considered in Gen2 CSP nitrate salt TES and Gen3 CSP chloride TES costs around \$1.5/kg (with a density of ~500 kg/m³). An example ceramic hollow sphere product is seemingly more expensive at \$2.2/kg. However, with a low density of ~140 kg/m³, the volumetric cost is \$308/m³ compared to \$750/m³ for the reference porous fire brick. This is the main motivation of this study – to understand the feasibility of using low-cost oxide-based cenospheres as thermal insulation for high-temperature liquids.

Now, we define a materials selection metric M to describe the cost-effectiveness of thermal insulation in Equation 1 where κ is thermal conductivity, ρ is the bulk density and C is cost of the insulation material. The higher the M value, the better the material is at providing cost-effective insulation.

$$M = \frac{1}{\kappa\rho C} \quad (1)$$

Table 1 summarizes the M values for two cenospheres, two hollow glass microspheres (HGMs), one reference porous insulation brick and one reference dense insulation brick that are both of interest to Gen2 and Gen3 CSP TES tank design. The high M values of cenospheres and HGMs suggest that they can be competitive to conventional insulation materials (e.g., highly porous firebricks). The M values also inversely correlate to the density of the materials as shown in Figure 1. It confirms the importance of lower densities because for a unit mass of an insulation material,³ a lower density implies more low-thermal-conductivity void volume.

Table 1. Calculated metric M for five materials including two cenospheres, two HGMs and one reference porous insulation brick. Larger M values are better.

Material	Product Category	Density	M
		kg/m ³	(W/m K) ⁻¹ ·(kg/m ³) ⁻¹ ·(\$/kg) ⁻¹
SphereOne XOL-200	Cenospheres	140	0.0590
CenoStar ES500		350	0.0113
3M iM30K	HGMs	600	0.0009
3M K1		125	0.0258
Reference Porous Insulation		500	0.0167

¹ The U.S. Department of Energy’s Gen3 CSP program is targeting a high temperature of 720°C.

² DOE’s target TES cost is \$15/kWh_{th} including total salt inventory, tank structure and foundation, internal and/or external insulation, internal piping, etc. where internal insulation usually cannot cost more than 30% of the total budget.

³ Quotes are usually provided by the refractory industry on a unit-weight basis.

Reference Dense Insulation	Conventional Refractories	2270	0.0007
----------------------------	---------------------------	------	--------

Because the cenospheres are fine, free-flowing particles, they can absorb the high-temperature TES medium and be fully saturated (similar to conventional porous fire bricks). Hence a barrier is needed to prevent this from happening. In the perfect scenario where the barrier does not fail, cenospheres should outperform conventional porous fire bricks because of their high M values. In the worst-case scenario where the barrier fails (which must be considered when designing a reliable TES system), cenospheres could still outperform conventional porous fire bricks because they can retain a large fraction of the air pockets to provide insulation assuming the hollow sphere structure is compatible with the TES medium. In contrast, conventional porous fire bricks with open and connected pore structures will be penetrated quickly by the TES medium hence losing most of their insulation performance. Therefore, the potential risk of a failed barrier and the fact that the simplified metric M does not take into account the service life of the materials in this worst-case scenario, compel one to investigate the chemical compatibility of cenospheres in a real TES medium.

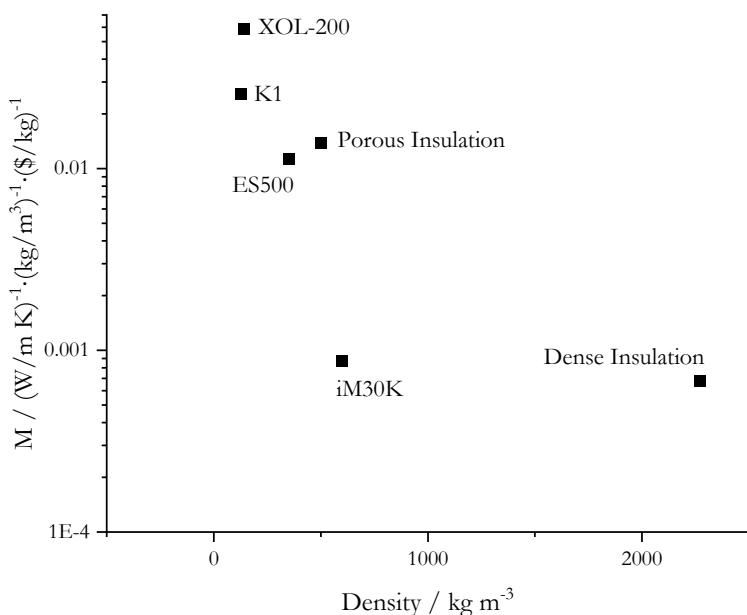


Figure 1. Correlation between the insulation metric M and the density of the materials analyzed.

2. Experimental

Materials: Two cenosphere products were used for chemical compatibility tests in molten nitrate salt at a composition used in commercial CSP plants (60 wt.% NaNO_3 /40 wt.% KNO_3). Both the NaNO_3 and KNO_3 were ACS reagent grade ($\geq 99\%$ purity) purchased from Alfa Aesar. CenoStar is a cenosphere with a higher Fe_2O_3 content typically seen in most commercially available products. Tarong is a special cenosphere sourced from Tarong Power Station in Australia with one of the lowest Fe_2O_3 content available to the market [77]. Table 2 summarizes the two types of cenosphere products and their chemical compositions, particle size, bulk density, and thermal conductivity at room temperature listed by the supplier, if available.

Table 2. Summary of tested cenosphere products.

Supplier	Product	Chemical Composition (wt.%)	Particle Size range (μm)	Bulk Density (g/cm^3)	Thermal Conductivity at Room Temperature (W/mK)
CenoStar	ES500	SiO ₂ : 50-60% Al ₂ O ₃ : 22-30% Fe ₂ O ₃ : 1.5-5%	5–500	0.32–0.45	0.1–0.2
Tarong Power Station	Tarong	SiO ₂ : 60-65% Al ₂ O ₃ : 30-35% Fe ₂ O ₃ : < 1%	25–250	~0.35	Not Available

SiO₂-Al₂O₃ binary phase diagram [78] suggests that the stable phases below 1595°C in both the CenoStar and Tarong cenospheres are SiO₂ and mullite. It has been found that cenospheres are made of an amorphous phase and a crystalline phase because of the general formation process [79]. Therefore, it is reasonable to assume that the amorphous phase is amorphous SiO₂ and the crystalline phase is mullite (see Section 3.2. Chemical Compatibility Tests for Low-Fe Cenospheres).

Chemical compatibility tests: Around 5–10 g of cenosphere particles were loaded into a dense alumina crucible (AL-4035, Advalue Technology) with at least 15 g of pre-mixed 60 wt.% NaNO₃/40 wt.% KNO₃ salt. The setup was then placed inside a muffle furnace (KSL-1200x, MTI) and heated up to 565°C⁴ at 5°C/min in ambient air for compatibility tests. No inert gas was used because commercial nitrate-salt tanks use air as their cover gas.

Survival rate by weight analysis: Because the bulk densities of the tested hollow spheres are all much less than 1 g/cm³ and the density of the molten nitrate at 565°C is about 1.7 g/cm³, the intact cenospheres will float in molten nitrate salt (or in water post chemical compatibility test). However, if they break due to chemical, thermal, and/or mechanical failures during the compatibility test, the sphere fragments will sink. A simple method to determine whether the tested products survive molten nitrate salt environment is to observe the floating vs. sinking behaviors at the test temperature as a function of time. After the immersion tests were completed, the molten salt and cenosphere mixture was cooled down. The retrieved mixture was dissolved in DI water to separate the floating particles from the sinking particles. To ensure complete dissolution of salt and avoid residual salt in the retrieved cenospheres that may affect various chemical analyses later, multiple DI water washes (each time with 400–500 ml of DI water) with stirring at 200–300 rpm for at least 20–30 minutes were used for a total of 20–30 g of salt/cenosphere mixture. With solubilities of 90 g/100 ml and 15 g/100 ml of water for NaNO₃ and KNO₃, respectively, a total of 1000–1500 ml of DI water wash for 40–60 minutes should remove most residual salt. The floating particles were collected with a pipette, filtered through 450-nm filter paper with additional fresh DI water, dried in a vacuum oven at 110°C and weighed to obtain the survival rate. The post-immersion particles were also analyzed with optical microscopy and scanning electron microscopy (SEM) with energy dispersive spectroscopy (EDS).

X-ray diffraction (XRD) and Fourier-transform infrared (FTIR) spectroscopy analyses: XRD and FTIR were performed on as-received and post-immersion cenospheres.

XRD was performed at 25°C on a PANalytical PW3040 X-ray diffractometer with a Cu-K α radiation (wavelength = 1.54 Å). The voltage and current of the generator were set to 45 kV and 40 mA, respectively.

⁴ 565°C is the operating temperature of the hot TES storage tank in current CSP power tower systems.

The XRD patterns were recorded in the 2θ range of 15.9944° to 89.9784° with a step size of 0.0170° and a scan step time of 29.845 s per degree. X'Pert HighScore Plus software was used to analyze the XRD patterns as well as perform Rietveld Refinement.

The FTIR measurement was performed on a Nicolet 6700 FTIR spectrometer with the OMNIC software package. The instrument was equipped with a Smart iTR diamond attenuated total reflectance (ATR). The spectra were collected at room temperature (1) with 50 scans of background data and 50 scans of experimental data, (2) between $4000\text{--}525\text{ cm}^{-1}$ at a resolution of 4.82 cm^{-1} using an optical velocity of 0.4747 cm/s , an aperture of 100% and a sample gain of 4, and (3) with advanced ATR correction and atmospheric suppression post-collection.

3. Results

3.1. Chemical Compatibility Tests for High-Fe Cenospheres

Figure 2(a) shows the image for as-received CenoStar ES500 cenospheres. The hollow structures can be seen from the image and almost no broken or fractured particles are found. We can also see variations in appearance such as particle shape and color. It qualitatively agrees with the expectations for cenospheres (i.e., a low-cost but non-optimized industrial by-product without intentional quality control). These features may serve as defects and have certain roles in the mechanical and chemical stabilities of the materials. Figure 2(b) shows the optical microscope image of CenoStar ES500 after 24 hours of compatibility test where cenosphere fragments are clearly seen. Density separation by flotation in DI water followed by weight analysis suggests that the survival rate is no more than 10%. The authors performed immersion tests on other commercially available cenospheres with similar Fe_2O_3 content.⁵ The results were similar.

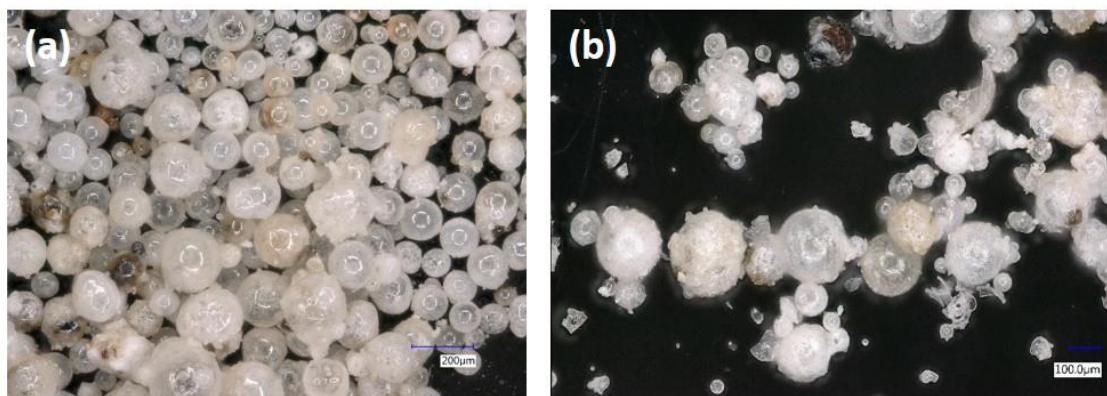


Figure 2. Optical images of (a) as-received CenoStar ES500 cenospheres and (b) post-immersion CenoStar ES500 cenospheres (24 hours).

Figure 3 shows the processed relative concentrations for the relevant cations of the as-received and post-immersion CenoStar ES500 cenospheres. The concentrations were average values by multiple EDS point scans on individual particles. Note that although the precision of the EDS scans was acceptable (with a standard deviation of 1-5 wt.% for each element), the true accuracy of the EDS scans was unknown, especially for oxygen because (1) no standards were used prior to quantification, and (2) the exact oxidation state of the major cations and whether the sample was fully oxidized is unknown. Therefore, the EDS measurement was intended more for qualitative understanding of the cenosphere chemistry. The results show a clear increase of Na and a decrease of Fe. The relative changes for other elements are less conclusive

⁵ Including the Fillite Series from Cary, SLG from Envirospheres, and Extendsphere SG and XOL-200 from SphereOne.

because the standard deviations were usually at least 1-2 wt.% based on five to ten point scans.

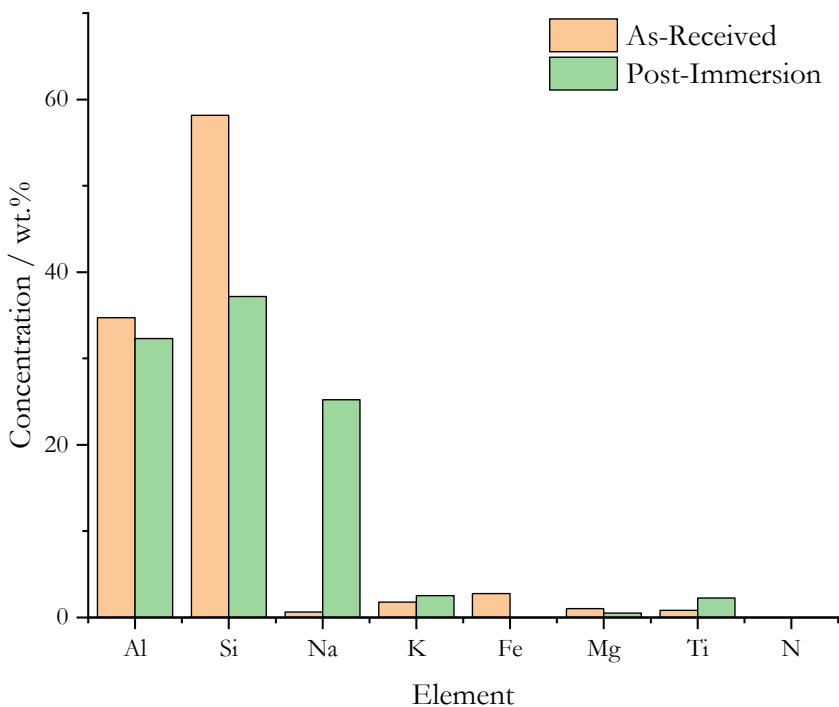


Figure 3. Concentrations of relevant elements in the as-received and post-immersion *CenoStar* cenospheres measured by EDS.

3.2. Chemical Compatibility Tests for Low-Fe Cenospheres

Figure 4 shows the optical microscope image for as-received and post-immersion (72 hours) Tarong cenospheres. There is little difference between the as-received and post-immersion states except for only a handful of small cenosphere fragments.

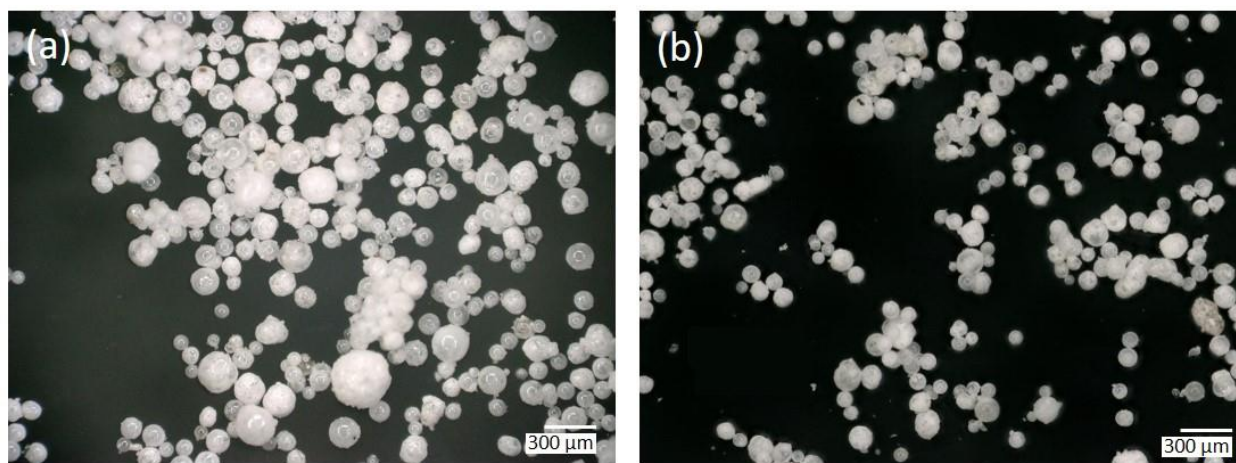


Figure 4. Optical images of (a) as-received Tarong cenospheres and (b) post-immersion Tarong cenospheres (72 hours).

Figure 5 shows the processed relative concentrations for the relevant cations of the as-received and post-immersion Tarong cenospheres. The concentrations were average values by multiple EDS point scans on

individual particles. The results again show a clear increase of Na and a decrease of Fe. A slight increase of Mg is also observed. The relative changes for other elements are less conclusive given the relative size of standard deviations.

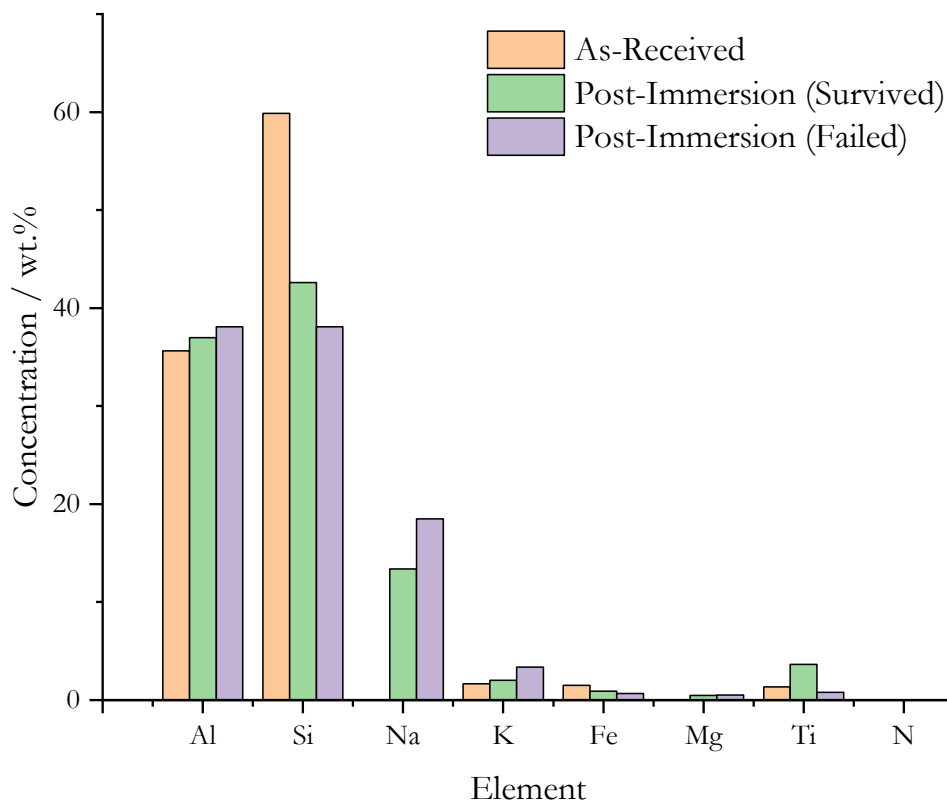


Figure 5. Concentrations of relevant elements in the as-received and post-immersion Tarong cenospheres measured by EDS.

Figure 6 shows the surviving percentage of the Tarong cenospheres at different particle size ranges as a function of immersion time up to 168 hours (7 days). The black dashed circles indicate the samples cooled inside the furnace where it takes at least 60 minutes for the salt temperature to change from 565°C to solidification at ~240°C. Otherwise, the samples were cooled outside the furnace, where it takes less than 10 minutes for the salt temperature to change from 565°C to solidification at ~240°C. The percentage of surviving particles of all tested commercially available high-Fe cenosphere products and a borosilicate-based glass microsphere product (iM30K from 3M) is given as a range for comparison.

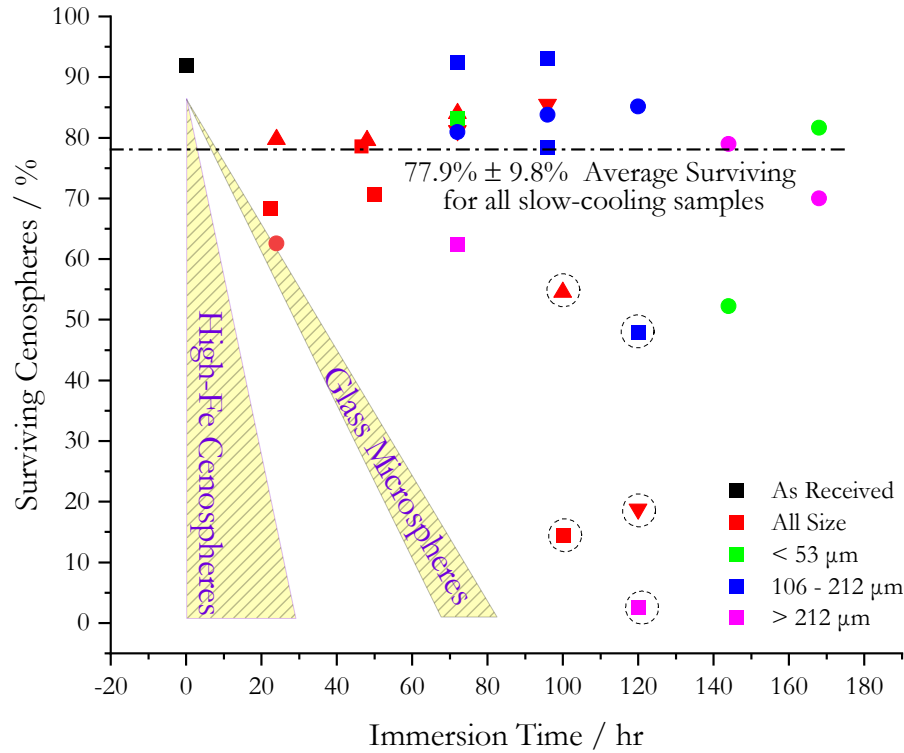


Figure 6. Percentage of surviving Tarong cenospheres after various periods of immersion in molten nitrate. Different shapes represent different experiments for the same particle size range tested. Black dashed circles represent furnace cooling condition; un-circled points were cooled outside the furnace at a faster rate. The yellow shaded regions represent the behaviors of all test high-Fe content cenosphere products and a 3M iM30K glass microsphere product.

Figure 7 shows the percentage of “unaccounted” cenospheres as a function of immersion time up to 120 hours. The mass of unaccounted cenospheres m_{unacct} is defined by Equation 2 as

$$m_{unacct} = m_i - m_s - m_f \quad (2)$$

where m_i is the initial total mass of cenospheres added to the immersion test, m_s is the total mass of surviving cenospheres, and m_f is the total mass of failed cenospheres. By definition, a positive value for m_{unacct} means mass loss of the cenosphere particles, while a negative value of m_{unacct} means a mass gain. However, this definition is not able to distinguish whether mass loss/gain occurs on the surviving or failed cenospheres. The “corrected zero mass change” line is set based on the mass change for the 0-hr immersion sample representing the manual collection error, i.e., systematic losses due to imperfect sample collection. Most of the data were generated by the same researcher to minimize variations of manual collection errors across different researchers. The trend in Figure 7 indicates increasing mass uptake by the cenospheres with molten salt exposure time.

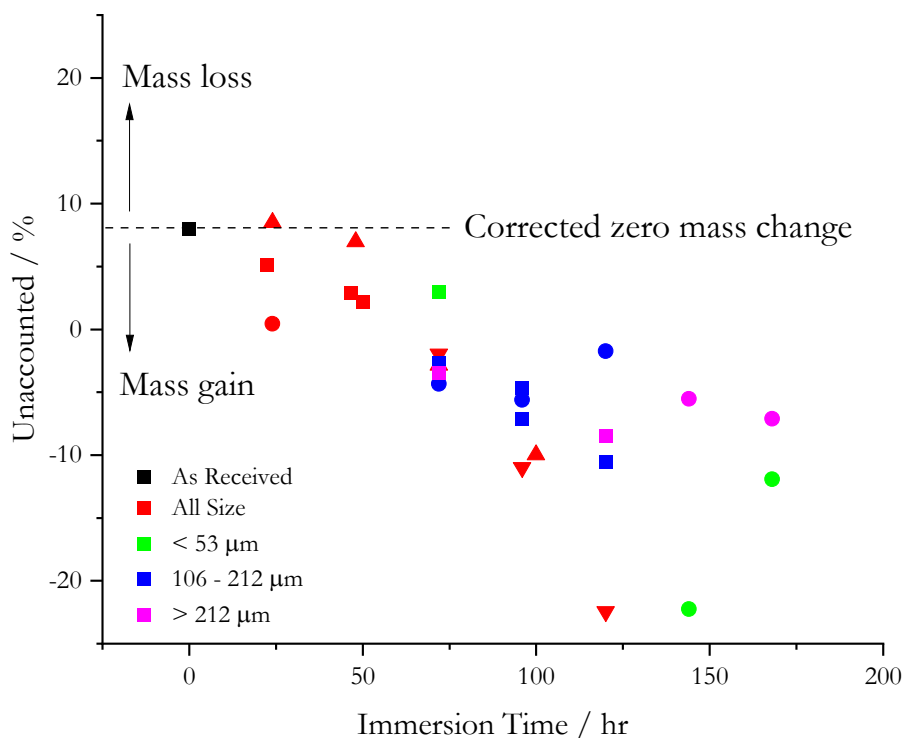


Figure 7. The percentage of unaccounted cenospheres after various periods of immersion in molten nitrate. Different shapes represent trials for the same particle size range tested.

Figure 8 shows the comparison of XRD patterns for as-received Tarong cenospheres without any salt immersion, and survived and failed Tarong cenospheres after 72-hr immersion in molten nitrate at 565°C. Figure 8(a) indicates that the as-received and surviving cenospheres are virtually the same with all major characteristic XRD reflection peaks and their relative intensities agreed. Almost all XRD crystalline reflection peaks are attributed to mullite and the amorphous hump around $2\theta = 18^\circ\text{--}27^\circ$ is attributed to amorphous silica. There are three observable differences for the failed Tarong cenospheres in Figure 8(b):

- 1) There are additional reflection peaks (indicated by the letters a-d). After excluding the mullite reflection peaks,⁶ the XRD database in X'Pert HighScore attributes peaks a and b to a potassium/sodium aluminosilicate species, $(\text{K},\text{Na})\text{AlSiO}_4$ or trikalsilite. Peaks c and d are attributed to a sodium aluminosilicate species, $\text{NaAlSi}_2\text{O}_6$ or jadeite. Note that there is an overlap between one of jadeite's reflection peaks and one of mullite's reflection peaks at peak d which may explain the enhancement around peak d.
- 2) There is a consistent shift of all major mullite reflection peaks towards lower 2θ angle by about 0.3° compared to those for the as-received and surviving cenospheres. The magnitude of the shift for the eight most intensive peaks increases slightly with the measured 2θ angle, from $0.289^\circ \pm 0.00843^\circ$ for the four major reflection peaks between 16° and 34° to $0.305^\circ \pm 0.0139^\circ$ for the other four major reflection peaks between 35° and 61° .
- 3) The amorphous SiO_2 hump seems to fade. However, the absolute intensity for the failed Tarong cenospheres is $\sim 50\%$ compared to that for the as-received and surviving Tarong cenospheres

⁶ It is certain that the mullite crystal structure is still the dominant crystal given the close match between the XRD reflection peaks in the failed Tarong cenospheres and the mullite reference pattern.

because the immersion experiments did not produce a high quantity of failed cenospheres (i.e., Figure 6 shows a 70–90% of survival rate). The decrease in the amorphous silica hump is

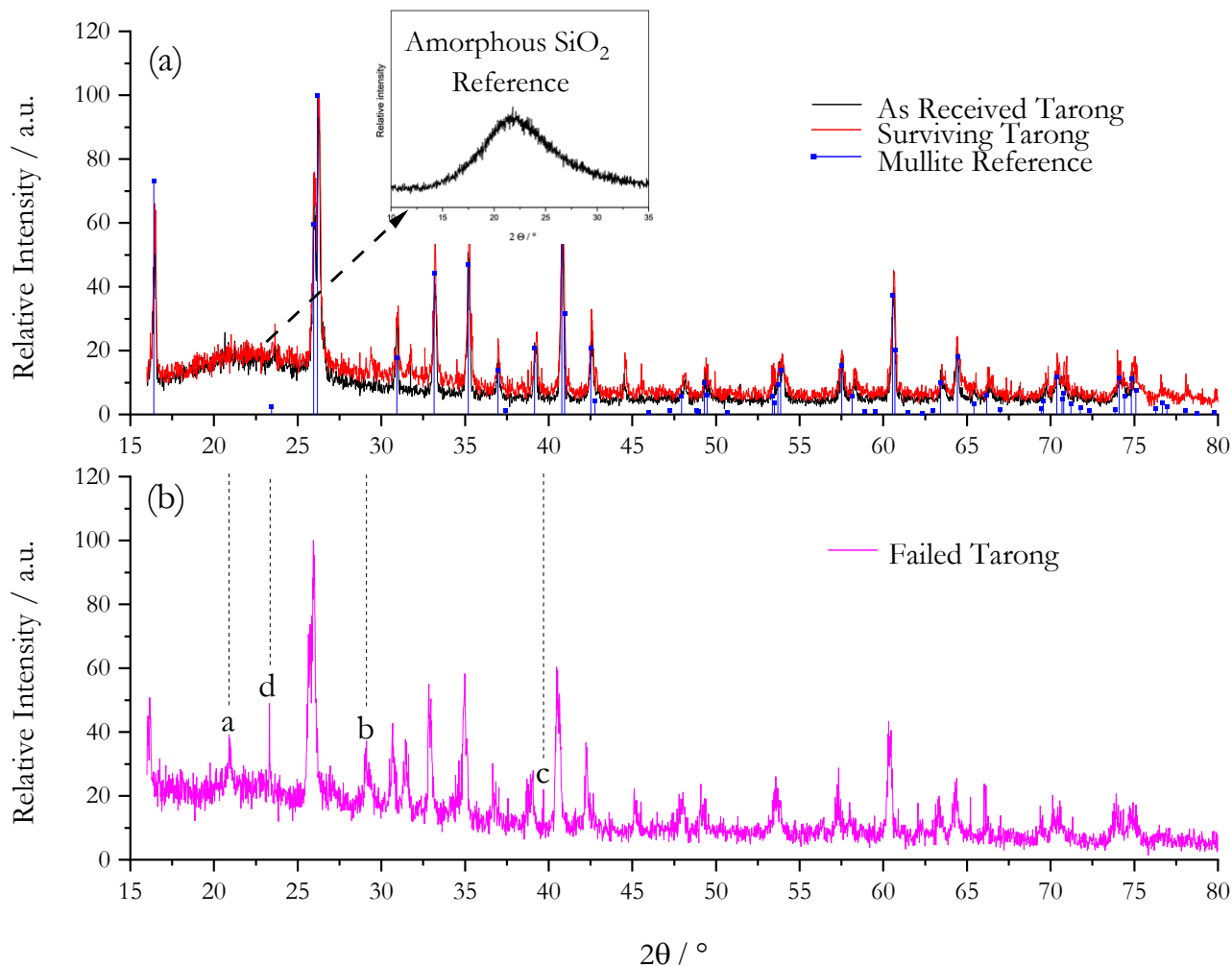


Figure 8. Comparison of XRD patterns for as-received, surviving (after 72-hr immersion) and failed (after 72-hr immersion) Tarong cenospheres. The letters a-d indicate additional peaks that appear in the failed cenosphere but cannot be attributed to mullite.

noteworthy, but the data must be interpreted cautiously and is not robust enough to make a quantitative conclusion.

Figure 9(a) shows the FTIR spectra for as-received Tarong cenospheres and Figure 9(b) shows the FTIR spectra for failed Tarong cenospheres after 72 hours and 288 hours of immersion. The letters indicate the

locations of different characteristic peaks (to be discussed in Section 4.2. Chemical Compatibility for Low-Fe Cenospheres).

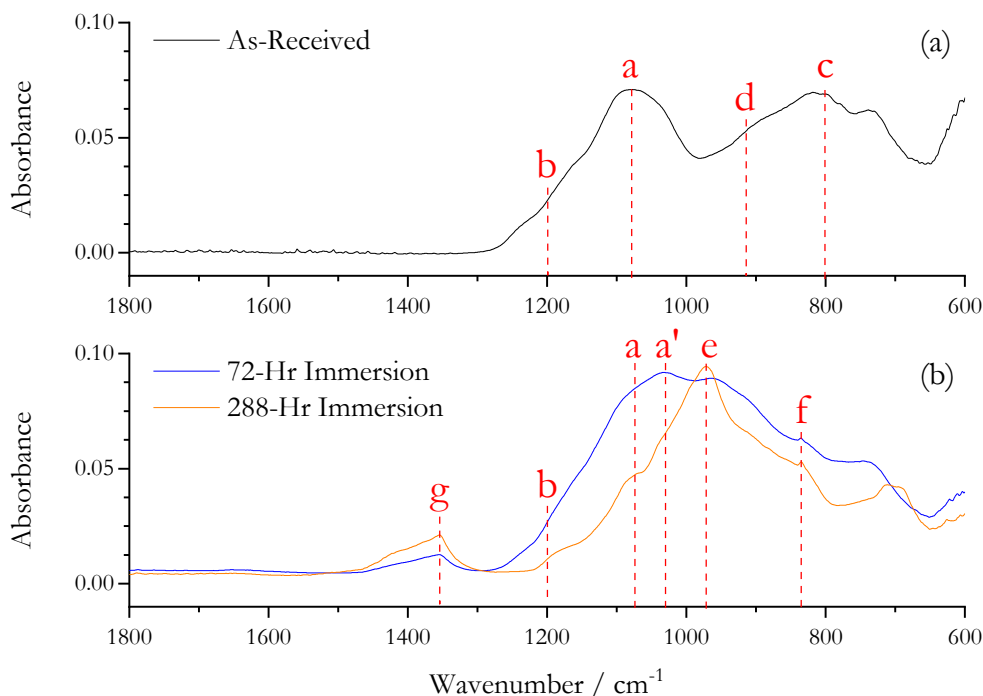


Figure 9. FTIR spectra for as-received Tarong cenospheres (top) and failed Tarong cenospheres after 72 hours and 288 hours of immersion (bottom). The letters indicate the locations of different characteristic peaks discovered.

4. Discussion

4.1. Chemical Compatibility for High-Fe Cenospheres

Although EDS should not be used as a quantitative characterization tool to precisely determine chemical compositions and composition changes, a significant decrease of Fe content from > 16 wt.% to 0 wt.% was observed in Figure 3. It suggests that the Fe species are not chemically stable in molten NaNO₃-KNO₃ at 565°C. Figure 10 shows the thermodynamic stability calculation of Fe₂O₃ in NaNO₃-KNO₃ in an atmosphere of 80% N₂ and 20% O₂ using HSC software. The calculation suggests a reaction of Fe₂O₃ with NaNO₃ to form NaFeO₂. The thermodynamic prediction also agrees with literature understanding which suggests Fe₂O₃ reacts with a trace amount of Na₂O in the molten NaNO₃-KNO₃ to form NaFeO₂ [80]–[82]. However, the chemical solubility of NaFeO₂ in molten NaNO₃/KNO₃ salt or whether it can form a perfect passivation layer to stop further reaction is not readily available in the literature. Therefore, if iron-oxide is indeed chemically unstable in the molten nitrate salts, it may act as local defects which weaken the integrity of the ceramic-based cenospheres.

Figure 2(b) shows the characteristics of a mechanical failure via fracture (e.g., sharp edges of the broken pieces) instead of a uniform dissolution. A potential reason for such fracture failure is the expansion of the gas pockets inside the hollow sphere structure when heated from room temperature to 565°C which leads to over-pressurization of the cenospheres. A simple spherical pressure vessel calculation suggests that approximately 30 atm of internal pressure is needed to break a cenosphere particle based on cenospheres'

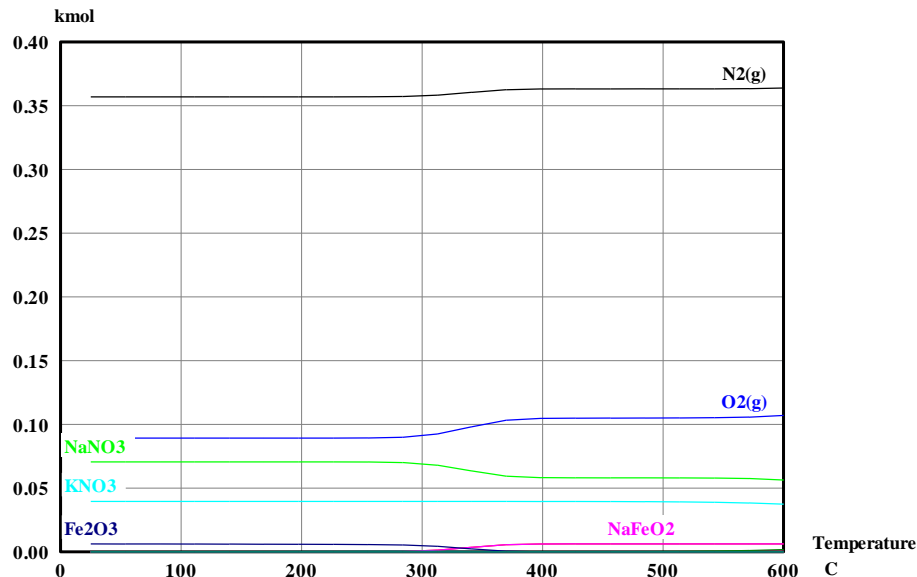


Figure 10. HSC prediction of thermodynamic stability of Fe_2O_3 in 60NaNO₃/40KNO₃ (wt.%).

compressive strength⁷ and wall thickness. 30 atm is ~10x higher than the pressure caused by the expansion of an ideal gas when heated from 25°C to 565°C. To confirm this, a separate experiment was conducted where the cenospheres were heated to 565°C without molten salt and held for over 24 hours. No particle fracture was observed which suggests that the strength of the as-received cenospheres can withstand stresses caused by internal pressurization up to 565°C. The observation agrees with the specification of the CenoStar ES500 cenospheres which states that the cenospheres have excellent temperature stability with a softening point of 1040°±5°C and a melting point of 1200°–1400°C.

Both the optical microscopy and EDS analysis above suggested that a typical cenosphere product with > 2 wt.% of Fe₂O₃ content does not have acceptable corrosion resistance to molten nitrate salt. The fracture of hollow particles during immersion is likely due to a combination of internal pressurization and molten salt immersion. For these reasons, the authors identified a low-Fe cenosphere product to focus on for further testing.

4.2. Chemical Compatibility for Low-Fe Cenospheres

The relative chemistry change for low-Fe Tarong cenospheres shown in Figure 5 is similar to that for high-Fe cenospheres. The major difference is the magnitude of the Na increase and Fe decrease which are both less for Tarong cenospheres. In addition, the chemistry of the survived cenospheres lies in between those of the as-received and failed suggesting that the survived cenospheres are not completely immune to chemistry change. Rather, they do sustain chemical attack from the salt but are more chemically resistant.

Two intriguing trends were observed in Figure 6:

- (1) The behaviors are very different simply based on the cooling methods. Samples of all sizes with faster cooling outside the furnace performed noticeably better than the ones with slower cooling inside the furnace (usually the last sample of an experiment series). The slower furnace cooling

⁷ No tensile strength information is available. Common knowledge suggests that the tensile strength of a ceramic-based oxide material is much lower than its compressive strength.

was unintentional because the last sample in an experiment series, usually started early in a week and finished in 4-5 days, was left inside the furnace for cooling over the weekend.

- (2) The low-Fe Tarong cenospheres, excluding all samples with slow furnace cooling, outperformed all the high-Fe cenospheres and borosilicate glass microspheres. Upon closer inspection of Figure 6, there was no clear advantage of a specific particle size range.

The results in Figure 6 are very encouraging because the data show a relatively flat trend with only some fluctuations up to 168 hours of immersion time. The average survival rate (excluding all furnace cooled samples) measured by weight analysis is $77.9\% \pm 9.8\%$.⁸ Our visual observation also suggests that most cenospheres were still floating in the molten salt inside the furnace prior to salt freezing and weight analysis. Because salt freezing (with $\sim 4.6\%$ of volume change [83]) prior to weight analysis could have damaged some cenospheres, the actual survival rate could be even higher. In addition, a periodic replenishment of salt in the crucibles to minimize salt dry-out due to evaporation is found to be an important empirical procedure to improve survival rate. It suggests that during real TES operation, the cenospheres that are fully immersed in molten salt could perform better because the chance for salt dry-out is very low.

The mass gain observed in Figure 7 is possibly due to 1) chemistry-related changes during salt immersion and/or 2) human error when collecting the particles after floatation and density separation. The consistent trend in Figure 7 towards mass gain from the “corrected zero mass change” line as a function of immersion time suggests that the mass gain is a result of chemical changes. Human error during collection should not be a function of immersion time and it should only produce a mass loss.⁹ The possible chemistry-related mass changes can also be categorized into two groups:

- 1) Alkaline and alkaline-earth metal and transition metal ions can diffuse and be inserted into the aluminosilicate network [84]–[90].
- 2) Simple salt permeation leads to salt trapped inside the cavities of the cenospheres. If the trapped salt is not dissolved during the floatation step, there will be mass gain. However, although trapped residual salt is a possibility, we did use extra precaution to remove any residual salt (see the procedures of multiple DI water washes/filtrations described in the Experimental section). Given the relatively high solubilities of the NaNO_3 and KNO_3 in water, we believe our experimental procedures were appropriate for us to refute such possibility of trapped salt. In addition, EDS on cross-sectioned cenospheres did not show any significant signals such as N from the nitrate ions that can be indicative of trapped salt on the inside of the cenospheres.

To further understand which is responsible for the mass gain, analytical characterizations with XRD and FTIR were performed.

The XRD results in Figure 8 have a few implications:

- 1) The new reflection peaks a-d in Figure 8(b) that are associated with sodium or potassium aluminosilicate species confirm that Na and K indeed chemically reacted with or diffused into the cenosphere structure.
- 2) The small shift for the mullite reflection peaks towards a lower 2θ angle can be a result of an increase in mullite crystal volume either due to insertion or doping of other ions [91]–[94] where the magnitude of the shift typically increases with the measurement angle 2θ as shown in Figure

⁸ If considering that samples without any immersion have a non-perfect survival rate of $\sim 92\%$ due to loss of manual collection, the actual survival rate for the immersed samples could be even higher.

⁹ As shown by the “as-received” data point in Figure 6 where the floatation and density separation were performed on as-received cenospheres without any molten salt immersion, the mass loss during manual collection error is about 8%.

11. Rietveld Refinement was also performed to analyze the micro-strain and crystallite size for the as-received, surviving and failed Tarong cenospheres based on their XRD patterns by comparing their structures to the standard mullite structure from the America Mineralogist Crystal Structure Database #0001059. The results show that the micro-strain increased from 0.013% in the as-received and surviving Tarong cenospheres to 0.023% in the failed Tarong cenospheres. This corroborates with the point above that the alkaline Na and K cations from the salt were incorporated into the cenospheres which caused the mullite phase to expand slightly to form “doped” mullite and the expansion was accompanied by more micro-strain and hence stress. Because K^+ ions (effective ionic radius of 1.37 angstrom [95]) are bigger than Na^+ ions (effective ionic radius of

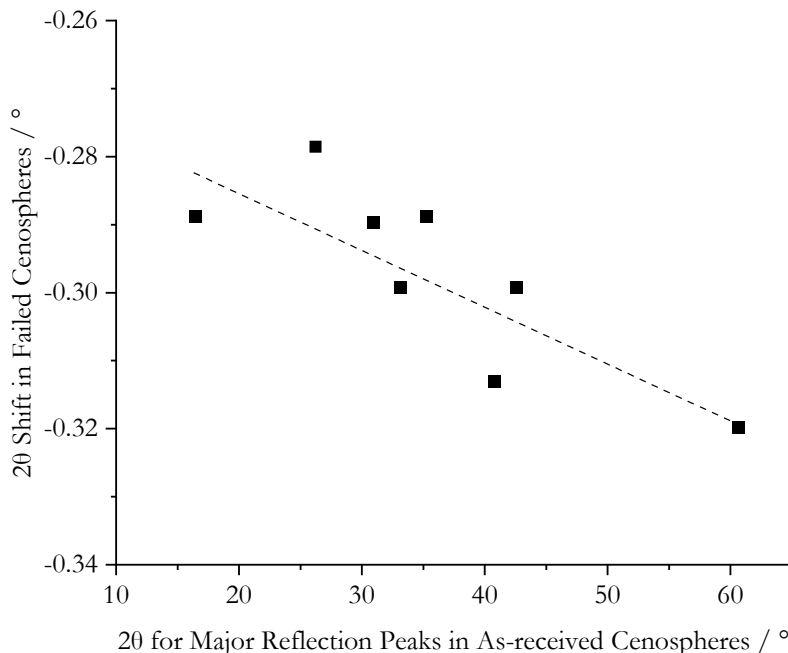


Figure 11. Relationship between the measured 2θ angles in the as-received cenospheres and the 2θ angle shift in the failed cenospheres after salt immersion. The dashed line indicates the best linear fit showing the increasing magnitude of the 2θ angle shift with increasing 2θ angle.

0.99 angstroms [95]), we hypothesize that it is easier for smaller Na^+ ions to diffuse into the cenosphere structure. Literature has shown that an even smaller Li^+ cation (ionic radius 0.59 angstrom [95]) diffuses more easily in a silicate structure [90]. The EDS analysis of the high-Fe CenoStar cenospheres after immersion (Figure 3) indirectly corroborates our hypothesis because it showed ~8–10 wt.% increase for Na and ~1–2 wt.% increase for K in the post-immersion cenospheres.

FTIR was used to analyze the changes of the alumino-silicate network in the cenospheres when Na and K cations are incorporated. The qualitative analysis was focused on the relative changes of bridging and non-bridging oxygens in the structure. The features of the FTIR results in Figure 9 are identified below.

For the as-received Tarong cenospheres:

- 1) Peak a at around 1075 cm^{-1} corresponds to asymmetric stretching vibrations of bridging oxygen bonds in a silica network [96]. It confirms the presence of amorphous SiO_2 as predicted by the Al_2O_3 - SiO_2 phase diagram and XRD measurements.
- 2) The small shoulder of peak b at $\sim 1200\text{ cm}^{-1}$ and peak c correspond to the wavenumber associated with bending of Si-O bonds in amorphous SiO_2 [97].
- 3) The small shoulder of peak d at $\sim 915\text{ cm}^{-1}$ corresponds to the presence of Al-O bonds in the octahedral form which is likely from the structure of mullite [98], [99].
- 4) The peaks in the range of $600\text{--}800\text{ cm}^{-1}$ may be ascribed to the stretching vibrations of tetrahedral Al-O bonds [100], [101].

Below are the features in the failed Tarong cenospheres:

- 1) Peak a, peak b, peak c indicate that amorphous SiO_2 is still present but at a lower intensity. It suggests that the amorphous SiO_2 is slightly modified.
- 2) Peak a' appears to result from the shifting of peak a from 1075 cm^{-1} . This is associated with a change in the Si-O-Si bond angle. The Si-O-Si bond angle differs as the number of oxygen atoms bonded to a given silicon atom changes, which could occur when bridging oxygens are broken [102].
- 3) Peak e at $\sim 960\text{--}970\text{ cm}^{-1}$ corresponds to a silicon atom with one non-bridging oxygen and peak f at $\sim 835\text{ cm}^{-1}$ corresponds to a silicon atom with two non-bridging oxygens [103], [104]
- 4) Peak g at $\sim 1360\text{ cm}^{-1}$ corresponds to the bonds in the nitrate anions [105]. Here we believe that the nitrate signal is not from residual salt.¹⁰ Instead, the nitrate anions serve to preserve overall charge neutrality by adhering to one of the Si atoms connected to the same bridging oxygen. Figure 12 illustrates the schematic of this process and shows how the charge neutrality is preserved by having the nitrate anions adhere to a Si^+ at a broken oxygen bond.

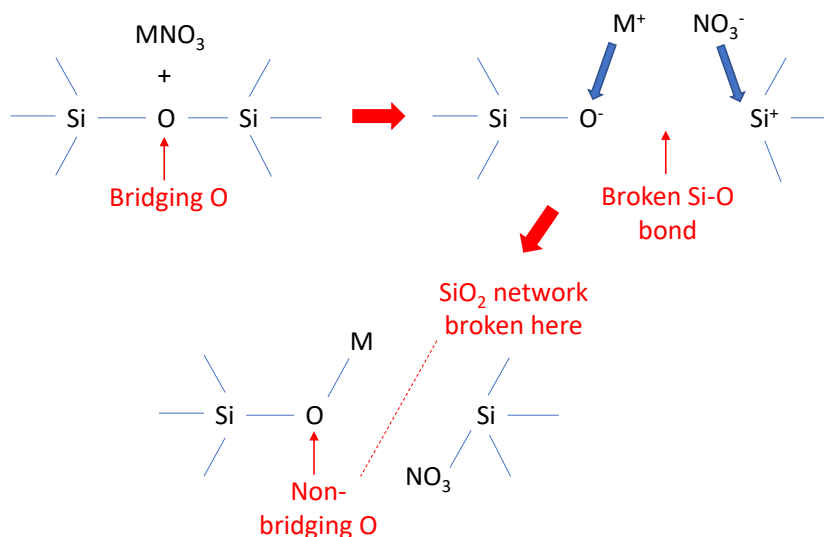


Figure 12. Schematic showing how a network modifier cation (M , assuming be $+1$ valency) breaks a bridging oxygen bond in a SiO_2 network and forms a non-bridging oxygen. The nitrate anion serves to preserve the overall charge neutrality by adhering to one of the Si atoms involved.

Although not every FTIR peak can be accurately and quantitatively accounted for given limited information, we can still see a qualitative trend where the peaks associated with bridging oxygen bonds (Si-O-Si) are fading from 1) the reduction of the intensity of peak a and shifting of peak a to peak a' and 2) the diminishing

¹⁰ Excessive water was used to clean the collected cenospheres to dissolve and remove salt residue.

of peaks b and c. Some bridging oxygens are believed to be converted to non-bridging oxygens due to the appearance of peak f and peak g. Figure 12 shows how normally each Si is bonded to four bridging oxygen to form a SiO₄ tetrahedral. When a bridging oxygen is converted to a non-bridging oxygen, the average number of oxygen atoms bonded to silicon atoms will change, leading to the appearance of peaks e and f in Figure 9. The FTIR data corroborate our hypothesis presented previously that cation attack from network modifiers such as Na⁺ and K⁺ in the molten salt occurred on the amorphous silica and mullite. The mullite phase likely experiences the cation attack to a lesser extent because mullite is known to have acceptable chemical stability in a similar molten salt environment [106], [107].

In summary, we believe that the conversion from bridging oxygens to non-bridging oxygens occurred due to the diffusion of the alkaline network modifier cations from the molten nitrate salt. These alkaline cations can diffuse tens of microns into a silicate structure [84]. Assuming cation attack on cenospheres by K and Na cations is due to diffusion at a similar order of magnitude, the entire cenosphere wall could be easily penetrated¹¹ leading to a volume expansion throughout the wall thickness. Combined with the observation of XRD reflection peak shifting which also indicates a volume expansion of the cenosphere microstructure, it suggests that the cenosphere particle walls can be subject to tension which eventually lead to fracture.

Now, we can speculate why low-Fe Tarong cenospheres behave significantly better than all other tested high-Fe cenospheres and glass microspheres. First, Fe³⁺ is usually a network modifier at lower concentrations [108]–[110]. Because of its 3+ valency, it means that three bridging oxygens need to be broken to accommodate one Fe³⁺ cation to preserve charge neutrality. Hence high-Fe cenospheres have a larger number of non-bridging oxygens, which means the strength of the network is reduced even before molten salt immersion. Therefore, the low-Fe Tarong cenospheres should have a stronger chemical network in the as-received state. It implies that the Tarong cenospheres have a higher tolerance of Na and K cation incorporation during salt immersion before a macroscopic failure/crack happens, which should directly translate to higher survival rates. Second, when Fe is lost from the cenosphere structure (as shown by both high-Fe and low-Fe cenospheres), it is unlikely that bridging oxygens will re-form. Hence the vacancies left by the loss of Fe may further weaken the structure. This is possibly another reason why the low-Fe Tarong cenospheres with smaller magnitude of Fe loss behaved better. Following the logic, we can speculate the following for a hypothetical cenosphere chemistry that could possess better chemical compatibility in molten nitrate salt:

- 1) A better cenosphere needs lower Fe, Ti, Ca, Mg, Na and K contents¹² in the as-received state. The network with fewer network modifier cations in the as-received state could tolerate more Na and K incorporation before macroscopic failure occurs. The stronger network also makes cation diffusion more difficult (i.e., a lower cation diffusivity due to a more closed-off structure) because pre-existing defects and flaws in the cenospheres could contribute to even faster cation diffusion [90].
- 2) A better cenosphere could benefit from a higher Al-to-Si ratio because a higher ratio tends to increase the fraction of mullite (which is less susceptible to network modification by certain cations [106], [107]) and reduce the fraction of amorphous SiO₂. At even higher Al₂O₃ content of above ~75 wt.%, Al₂O₃ and mullite will form instead of Al₂O₃ and SiO₂ based on the Al₂O₃-SiO₂ phase diagram [78].

4.3. Implications and Future Work

From the safe operation perspective, fail-safe is a top priority for molten salt based TES design. It requires

¹¹ Cenospheres usually have a wall thickness of < 5 μm.

¹² All these elements could serve as network modifiers.

that the insulation remains thermally insulating under different potential failure modes, e.g., wetting by the molten salt. The cenosphere insulation concept is of particular interest in this respect. The free-flowing cenosphere particles require a containment structure, which may also serve as a barrier to prevent salt permeation. With one of the highest M values, cenospheres are the most cost-effective thermal insulation materials compared to conventional porous fire bricks which also require a barrier or containment to prevent salt permeation. In the extreme event where the barrier or containment fails, the cenospheres could retain most of their physical structure and some thermal insulation properties due to the presence of air pockets in the hollow sphere structure. In the worst-case scenario, the chemical resistance of the cenospheres to molten nitrate salt degrades gradually over time, allowing the TES operator to respond to detected containment failure and perform emergency procedures to gradually cease operation. The authors are currently investigating a cenosphere insulation prototype with a stainless-steel containment which will provide more insight into the real-world applicability and cost of the concept.

5. Conclusions

The concept of using cenospheres as thermal insulation material in molten nitrate salt is presented. The chemical compatibility analysis suggests that

- 1) Low-Fe (< 1 wt.% Fe_2O_3) cenospheres have an average survival rate that is significantly higher than cenospheres with higher iron content (1.5-5 wt.%), measured as $77.9\% \pm 9.8\%$ up to 7 days of immersion in molten 60 wt.% $\text{NaNO}_3/40$ wt.% KNO_3 salt vs. less than 10% within 1 day of immersion.
- 2) Cation diffusion (e.g., due to the alkaline, network-modifier cations such as Na^+ and K^+ from the salt) occurred in the cenosphere structure, which is supported by the weight analysis, EDS, XRD and FTIR measurements. The incorporation of the network modifiers caused volume expansion of the microstructure and the formation of non-bridging oxygens. Both factors weaken the microstructure which eventually leads to macroscopic fracture of the cenosphere particles during molten nitrate salt immersion.
- 3) The presence of iron in the as-received cenospheres could contribute to network modification of the amorphous silica network before salt immersion. As cation diffusion is a function of diffusivity, a more open and modified cenosphere structure is more susceptible to such chemical attack. This is postulated as the reason why the low-iron Tarong cenospheres behaved better than other cenospheres, i.e., because Tarong cenospheres started with a stronger network and could tolerate more network modification before macroscopic failure via cracking.

The chemical compatibility analysis also points to a future path towards engineering a more resistant chemistry for hollow microspheres, which may be necessary if the industrial byproduct cenospheres do not meet all the compatibility requirements as an insulation material for molten salt TES.

Acknowledgement

This work was authored by the National Renewable Energy Laboratory, operated by Alliance for Sustainable Energy, LLC, for the U.S. Department of Energy (DOE) under Contract No. DE-AC36-08GO28308. Funding was provided by U.S. Department of Energy Office of Energy Efficiency and Renewable Energy, Solar Energy Technologies Office (Award number DE-EE00037877). The views expressed in the article do not necessarily represent the views of the DOE or the U.S. Government. The U.S. Government retains and the publisher, by accepting the article for publication, acknowledges that the U.S. Government retains a nonexclusive, paid-up, irrevocable, worldwide license to publish or reproduce the published form of this work, or allow others to do so, for U.S. Government purposes. The authors gratefully acknowledge Prof. Ted Steinberg from Queensland University of Technology and Tarong Power Station for supplying the Tarong cenosphere samples.

References

- [1] M. Mehos *et al.*, “Concentrating Solar Power Best Practices,” 2020. doi: 10.1016/b978-0-12-819970-1.00020-7.
- [2] M. Mehos *et al.*, “Concentrating Solar Power Gen3 Demonstration Roadmap,” 2017. doi: 10.2172/1338899.
- [3] W. D. Steinmann, H. Jockenhöfer, and D. Bauer, “Thermodynamic Analysis of High-Temperature Carnot Battery Concepts,” *Energy Technol.*, vol. 8, no. 3, p. 1900895, 2020, doi: 10.1002/ente.201900895.
- [4] A. Pillai, A. Kaya, M. De Paepe, and S. Lecompte, “Performance Analysis of An Organic Rankine Cycle for Integration in A Carnot Battery,” in *Proceedings of the 5th International Seminar on ORC Power Systems*, 2019.
- [5] D. R. Smith, J. G. Hust, and L. J. Van Poolen, “Effective Thermal Conductivity of A Glass Fiberblanket Standard Reference Material,” Boulder, CO, 1981.
- [6] K. E. Wilkes and P. W. Childs, “Thermal Performance of Fiberglass and Cellulose Attic Insulations,” 1992.
- [7] R. P. Tye, A. O. Desjarlais, D. W. Yarbrough, and D. L. McElroy, “An Experimental Study of Thermal Reistance Values (R-Values) of Low-Density Mineral-Fiber Building Insulation Batts Commercially Available in 1977,” 1980.
- [8] C. Q. Hong, J. C. Han, X. H. Zhang, and J. C. Du, “Novel nanoporous silica aerogel impregnated highly porous ceramics with low thermal conductivity and enhanced mechanical properties,” *Scr. Mater.*, vol. 68, no. 8, pp. 599–602, Apr. 2013, doi: 10.1016/j.scriptamat.2012.12.015.
- [9] Y. Han, C. Li, C.-A. Wang, C. Bian, and S. Li, “Porous anorthite ceramics with ultra-low thermal conductivity,” *Artic. J. Eur. Ceram. Soc.*, vol. 33, pp. 2573–2578, 2013, doi: 10.1016/j.jeurceramsoc.2013.04.006.
- [10] L. Gong, Y. Wang, X. Cheng, R. Zhang, and H. Zhang, “Thermal conductivity of highly porous mullite materials,” *Int. J. Heat Mass Transf.*, vol. 67, pp. 253–259, 2013, doi: 10.1016/j.ijheatmasstransfer.2013.08.008.
- [11] R. Barea, M. I. Osendi, J. M. F. Ferreira, and P. Miranzo, “Thermal conductivity of highly porous mullite material,” *Acta Mater.*, vol. 53, no. 11, pp. 3313–3318, 2005, doi: 10.1016/j.actamat.2005.03.040.
- [12] L. Wu, C. Li, J. Yang, and H. Li, “Fabrication and properties of porous anorthite/mullite ceramics with both high porosity and high strength,” *Int. J. Appl. Ceram. Technol.*, vol. 16, no. 6, pp. 2197–2205, 2019, doi: 10.1111/ijac.13275.
- [13] K. W. Schlichting, N. P. Padture, and P. G. Klemens, “Thermal conductivity of dense and porous yttria-stabilized zirconia,” *J. Mater. Sci.*, vol. 36, no. 12, pp. 3003–3010, 2001, doi: 10.1023/A:1017970924312.
- [14] C. Li, Y. Han, L. Wu, K. Chen, and L. nan An, “Fabrication and properties of porous anorthite ceramics with modelling pore structure,” *Mater. Lett.*, vol. 190, pp. 95–98, 2017, doi: 10.1016/j.matlet.2016.12.131.
- [15] D. Li and M. Li, “Porous Y_2SiO_5 Ceramic with Low Thermal Conductivity,” *J. Mater. Sci. Technol.*, vol. 28, no. 9, pp. 799–802, 2012, doi: 10.1016/S1005-0302(12)60133-9.

- [16] J. Feng, J. Feng, Y. Jiang, and C. Zhang, "Ultralow density carbon aerogels with low thermal conductivity up to 2000 °C," *Mater. Lett.*, vol. 65, no. 23–24, pp. 3454–3456, 2011, doi: 10.1016/j.matlet.2011.07.114.
- [17] G. Wei, Y. Liu, X. Zhang, F. Yu, and X. Du, "Thermal conductivities study on silica aerogel and its composite insulation materials," *Int. J. Heat Mass Transf.*, vol. 54, no. 11–12, pp. 2355–2366, 2011, doi: 10.1016/j.ijheatmasstransfer.2011.02.026.
- [18] L. An *et al.*, "An all-ceramic, anisotropic, and flexible aerogel insulation material," *Nano Lett.*, vol. 20, no. 5, pp. 3828–3835, 2020, doi: 10.1021/acs.nanolett.0c00917.
- [19] D. M. Smith, A. Maskara, and U. Boes, "Aerogel-based thermal insulation," *J. Non. Cryst. Solids*, vol. 225, no. 1–3, pp. 254–259, 1998, doi: 10.1016/S0022-3093(98)00125-2.
- [20] D. Lee, P. C. Stevens, S. Q. Zeng, and A. J. Hunt, "Thermal characterization of carbon-opacified silica aerogels," *J. Non. Cryst. Solids*, vol. 186, pp. 285–290, 1995, doi: 10.1016/0022-3093(95)00055-0.
- [21] R. Baetens, B. P. Jelle, and A. Gustavsen, "Aerogel insulation for building applications: A state-of-the-art review," *Energy Build.*, vol. 43, no. 4, pp. 761–769, 2011, doi: 10.1016/j.enbuild.2010.12.012.
- [22] Z. Ignaszak, A. Baranowski, J. Hycnar, and M. Zak, "Heat-Insulating, High-Temperature Materials on Cenosphere Base," in *Insulation Materials, Testing and Applications*, D. McElroy and J. Kimpflen, Eds. West Conshohocken, PA: ASTM International, pp. 741–747.
- [23] V. B. Fenelonov, M. S. Mel'gunov, and V. N. Parmon, "The properties of cenospheres and the mechanism of their formation during high-temperature coal combustion at thermal power plants," *KONA Powder Part. J.*, vol. 28, no. 28, pp. 189–208, 2010, doi: 10.14356/kona.2010017.
- [24] Y. Liao, X. Wu, H. Liu, and Y. Chen, "Thermal conductivity of powder silica hollow spheres," *Thermochim. Acta*, vol. 526, no. 1–2, pp. 178–184, Nov. 2011, doi: 10.1016/j.tca.2011.09.011.
- [25] Y. Bao, Q. L. Kang, J. Z. Ma, and C. Liu, "Monodisperse hollow TiO₂ spheres for thermal insulation materials: Template-free synthesis, characterization and properties," *Ceram. Int.*, vol. 43, no. 12, pp. 8596–8602, Aug. 2017, doi: 10.1016/j.ceramint.2017.03.155.
- [26] T. Gao, B. P. Jelle, L. I. C. Sandberg, and A. Gustavsen, "Monodisperse hollow silica nanospheres for nano insulation materials: Synthesis, characterization, and life cycle assessment," *ACS Appl. Mater. Interfaces*, vol. 5, no. 3, pp. 761–767, Feb. 2013, doi: 10.1021/am302303b.
- [27] J. Ding, Q. Liu, B. Zhang, F. Ye, and Y. Gao, "Preparation and characterization of hollow glass microsphere ceramics and silica aerogel/hollow glass microsphere ceramics having low density and low thermal conductivity," *J. Alloys Compd.*, vol. 831, p. 154737, Aug. 2020, doi: 10.1016/j.jallcom.2020.154737.
- [28] P. Hao-Qiang, Z. Hu, L. Zeng-Yao, and T. Wen-Quan, "Experimental Study on the Thermal Insulating Performance of Silica Aerogel Composite," *J. Eng. Thermophys.*, vol. 39, no. 1, 2018.
- [29] T. Xie, Y. L. He, and Z. J. Hu, "Theoretical study on thermal conductivities of silica aerogel composite insulating material," *Int. J. Heat Mass Transf.*, vol. 58, no. 1–2, pp. 540–552, Mar. 2013, doi: 10.1016/j.ijheatmasstransfer.2012.11.016.
- [30] V. Rheinheimer *et al.*, "Multi-scale study of high-strength low-thermal-conductivity cement composites containing cenospheres," *Cem. Concr. Compos.*, vol. 80, pp. 91–103, 2017, doi: 10.1016/j.cemconcomp.2017.03.002.

- [31] Y. Wu, J. Y. Wang, P. J. M. Monteiro, and M. H. Zhang, "Development of ultra-lightweight cement composites with low thermal conductivity and high specific strength for energy efficient buildings," *Constr. Build. Mater.*, vol. 87, pp. 100–112, 2015, doi: 10.1016/j.conbuildmat.2015.04.004.
- [32] A. Hanif, Z. Lu, and Z. Li, "Utilization of fly ash cenosphere as lightweight filler in cement-based composites – A review," *Construction and Building Materials*, vol. 144. Elsevier Ltd, pp. 373–384, Jul. 30, 2017, doi: 10.1016/j.conbuildmat.2017.03.188.
- [33] A. Hanif, S. Diao, Z. Lu, T. Fan, and Z. Li, "Green lightweight cementitious composite incorporating aerogels and fly ash cenospheres - Mechanical and thermal insulating properties," *Constr. Build. Mater.*, vol. 116, pp. 422–430, 2016, doi: 10.1016/j.conbuildmat.2016.04.134.
- [34] X. Huang, R. Ranade, Q. Zhang, W. Ni, and V. C. Li, "Mechanical and thermal properties of green lightweight engineered cementitious composites," *Constr. Build. Mater.*, vol. 48, pp. 954–960, 2013, doi: 10.1016/j.conbuildmat.2013.07.104.
- [35] W. Wang, C. Lu, Y. Li, and Q. Li, "An investigation on thermal conductivity of fly ash concrete after elevated temperature exposure," *Constr. Build. Mater.*, vol. 148, pp. 148–154, 2017, doi: 10.1016/j.conbuildmat.2017.05.068.
- [36] H. Zhou and A. L. Brooks, "Thermal and mechanical properties of structural lightweight concrete containing lightweight aggregates and fly-ash cenospheres," *Constr. Build. Mater.*, vol. 198, pp. 512–526, 2019, doi: 10.1016/j.conbuildmat.2018.11.074.
- [37] A. Chávez-Valdez, A. Arizmendi-Morquecho, G. Vargas, J. M. Almanza, and J. Alvarez-Quintana, "Ultra-low thermal conductivity thermal barrier coatings from recycled fly-ash cenospheres," *Acta Mater.*, vol. 59, no. 6, pp. 2556–2562, Apr. 2011, doi: 10.1016/j.actamat.2011.01.011.
- [38] Y. Liao, X. Wu, Z. Wang, R. Yue, G. Liu, and Y. Chen, "Composite thin film of silica hollow spheres and waterborne polyurethane: Excellent thermal insulation and light transmission performances," *Mater. Chem. Phys.*, vol. 133, no. 2–3, pp. 642–648, Apr. 2012, doi: 10.1016/j.matchemphys.2012.01.041.
- [39] I. Panchenko, M. Akulova, and D. Panchenko, "Thermal insulation coating based on water-based polymer dispersion," *MATEC Web Conf.*, vol. 143, p. 02007, 2018, doi: 10.1051/mateconf/201814302007.
- [40] J. Wang, Y. Tian, and J. Zhang, "Thermal insulating epoxy composite coatings containing sepiolite/hollow glass microspheres as binary fillers: Morphology, simulation and application," *Sci. Eng. Compos. Mater.*, vol. 24, no. 3, pp. 379–386, May 2017, doi: 10.1515/secm-2014-0397.
- [41] Q. Kang, Y. Bao, M. Li, and J. Ma, "Effect of wall thickness of hollow TiO₂ spheres on properties of polyacrylate film: Thermal insulation, UV-shielding and mechanical property," *Prog. Org. Coatings*, vol. 112, pp. 153–161, Nov. 2017, doi: 10.1016/j.porgcoat.2017.04.045.
- [42] Y. Bao, R. Guo, and J. Ma, "Hierarchical Flower-Like Hollow SiO₂@TiO₂ Spheres with Enhanced Thermal Insulation and Ultraviolet Resistance Performances for Building Coating," *ACS Appl. Mater. Interfaces*, vol. 12, no. 21, pp. 24250–24261, May 2020, doi: 10.1021/acsami.0c03125.
- [43] L. M. Aksel'rod, Z. E. Goryacheva, N. A. Chuprina, L. Y. Kizel'shtejn, and A. L. Shpitsgluz, "Heat-insulating and radiotransparent ceramics on the base of aluminosilicate microspheres," *Refract. Ind. Ceram.*, vol. 37, no. 9–10, pp. 337–340, 1996, Accessed: Jul. 13, 2020. [Online]. Available: <https://link.springer.com/content/pdf/10.1007/BF02238689.pdf>.

- [44] N. M. Barkoula, B. Alcock, N. O. Cabrera, and T. Peijs, "Flame-Retardancy Properties of Intumescent Ammonium Poly(Phosphate) and Mineral Filler Magnesium Hydroxide in Combination with Graphene," *Polym. Polym. Compos.*, vol. 16, no. 2, pp. 101–113, 2008, doi: 10.1002/pc.
- [45] J. Brown, J. Oldenkamp, R. Gamache, D. Grbovic, and E. Kartalov, "Hollow-microsphere composite offers depth-independent superior thermal insulation for diver suits," *Mater. Res. Express*, vol. 6, no. 5, 2019, doi: 10.1088/2053-1591/ab0447.
- [46] C. Li *et al.*, "Thermo-physical properties of polyester fiber reinforced fumed silica/hollow glass microsphere composite core and resulted vacuum insulation panel," *Energy Build.*, vol. 125, pp. 298–309, Aug. 2016, doi: 10.1016/j.enbuild.2016.05.013.
- [47] R. Liao, F. Zhang, Y. Yuan, L. Yang, T. Liu, and C. Tang, "Preparation and Electrical Properties of Insulation Paper Composed of SiO₂ Hollow Spheres," *Energies*, vol. 5, no. 8, pp. 2943–2951, Aug. 2012, doi: 10.3390/en5082943.
- [48] E. Pakdel *et al.*, "Functional cotton fabric using hollow glass microspheres: Focus on thermal insulation, flame retardancy, UV-protection and acoustic performance," *Prog. Org. Coatings*, vol. 141, p. 105553, Apr. 2020, doi: 10.1016/j.porgcoat.2020.105553.
- [49] A. T. Kulesa and M. J. Robinson, "Analytical study of structural thermal insulating syntactic foams," *Compos. Struct.*, vol. 119, pp. 551–558, Jan. 2015, doi: 10.1016/j.compstruct.2014.09.025.
- [50] R. Zhang, J. Feng, X. Cheng, L. Gong, Y. Li, and H. Zhang, "Porous thermal insulation materials derived from fly ash using a foaming and slip casting method," *Energy Build.*, vol. 81, pp. 262–267, 2014, doi: 10.1016/j.enbuild.2014.06.028.
- [51] C. Zhang, C. Zhang, R. Huang, and X. Gu, "Effects of hollow microspheres on the thermal insulation of polysiloxane foam," *J. Appl. Polym. Sci.*, vol. 134, no. 18, May 2017, doi: 10.1002/app.44778.
- [52] D. Winkel, S. Seibel, R. Puffer, and A. Schnettler, "Investigation of the Thermal Conductivity of Syntactic Foam at 77 K," *IEEE Trans. Appl. Supercond.*, vol. 26, no. 3, Apr. 2016, doi: 10.1109/TASC.2016.2548358.
- [53] Q. Peng *et al.*, "Superlight, Mechanically Flexible, Thermally Superinsulating, and Antifrosting Anisotropic Nanocomposite Foam Based on Hierarchical Graphene Oxide Assembly," *ACS Appl. Mater. Interfaces*, vol. 9, no. 50, pp. 44010–44017, Dec. 2017, doi: 10.1021/acsami.7b14604.
- [54] C. Huang, Z. Huang, and Q. Wang, "Effect of high-temperature treatment on the mechanical and thermal properties of phenolic syntactic foams," *Polym. Eng. Sci.*, vol. 58, no. 12, pp. 2200–2209, Dec. 2018, doi: 10.1002/pen.24835.
- [55] J. H. Bae, B. K. Hwang, J. H. Kim, S. K. Kim, and J. M. Lee, "Cumulative damage of hollow glass microsphere weight fraction in polyurethane foam in response to cryogenic temperatures and repeated impact loading," *Cryogenics (Guildf.)*, vol. 107, p. 103057, Apr. 2020, doi: 10.1016/j.cryogenics.2020.103057.
- [56] A. L. Brooks, Z. Shen, and H. Zhou, "Development of a high-temperature inorganic synthetic foam with recycled fly-ash cenospheres for thermal insulation brick manufacturing," *J. Clean. Prod.*, vol. 246, p. 118748, Feb. 2020, doi: 10.1016/j.jclepro.2019.118748.
- [57] O. Selivanov, V. Chukhlanov, and M. Ilina, "Development of energy-efficient heat-insulating foam," in *International Scientific Conference "Construction and Architecture: Theory and*

- Practice for the Innovation Development*” (CATPID-2019), 2019, vol. 138, p. 01012, doi: 10.1051/e3sconf/201913801012.
- [58] G. T. Kim *et al.*, “Investigations on thermal energy transfer between two contrasting media and its application to protect skin burn,” *Int. J. Therm. Sci.*, vol. 153, p. 106364, Jul. 2020, doi: 10.1016/j.ijthermalsci.2020.106364.
- [59] A. Das and B. K. Satapathy, “Structural, thermal, mechanical and dynamic mechanical properties of cenosphere filled polypropylene composites,” *Mater. Des.*, vol. 32, no. 3, pp. 1477–1484, 2011, doi: 10.1016/j.matdes.2010.08.041.
- [60] J. Feng, R. Zhang, L. Gong, Y. Li, W. Cao, and X. Cheng, “Development of porous fly ash-based geopolymer with low thermal conductivity,” *Mater. Des.*, vol. 65, pp. 529–533, 2015, doi: 10.1016/j.matdes.2014.09.024.
- [61] S. Huo, J. Wang, and X. Wu, “Morphology, thermal and mechanical performances of SR composites containing sepiolite and HGMs as binary fillers,” *J. Polym. Eng.*, vol. 37, no. 2, pp. 197–204, Feb. 2017, doi: 10.1515/polyeng-2015-0442.
- [62] B. Ravichandran and M. Sasikumar, “Mechanical, Ablative, and Thermal Properties of Cenosphere-Filled Ceramic/Phenolic Composites,” *Polym. Compos.*, vol. 37, no. 6, pp. 1906–1913, 2016, doi: 10.1002/pc.10.1002/pc.
- [63] A. S. Filimonov, V. A. Tarasov, M. A. Komkov, V. A. Moiseev, M. P. Timofeev, and R. V. Boyarskaya, “An Experimental Assessment of Synergism between Binders and Glass Microspheres when Creating Composite Thermal Insulation Materials,” *Polym. Sci. Ser. D*, vol. 9, no. 3, pp. 30–34, 2016, doi: 10.1134/S1995421216030072.
- [64] M. Bahrami, Z. Ranjbar, R. A. Khosroshahi, and S. Ashhari, “Investigating corrosion protection properties of epoxy thermal insulators through cyclic corrosion test,” *Prog. Org. Coatings*, vol. 113, pp. 25–30, Dec. 2017, doi: 10.1016/j.porgcoat.2017.07.021.
- [65] H. Yang *et al.*, “Mechanical, Thermal and Fire Performance of An Inorganic–Organic Insulation Material Composed of Hollow Glass Microspheres and Phenolic Resin,” *J. Colloid Interface Sci.*, vol. 530, pp. 163–170, 2018, doi: 10.1016/j.jcis.2018.06.075.
- [66] Y. Bian, Y. Kwon, and J. S. Kim, “Thermal and mechanical properties of polyurethane composites filled with thermally expanded hollow microspheres,” 2018.
- [67] X.-W. Zhao, C.-G. Zang, Y.-L. Sun, Y.-L. Zhang, Y.-Q. Wen, and Q.-J. Jiao, “Effect of hybrid hollow microspheres on thermal insulation performance and mechanical properties of silicone rubber composites,” *J. Appl. Polym. Sci.*, vol. 135, no. 11, p. 46025, Mar. 2018, doi: 10.1002/app.46025.
- [68] S. Nath, H. Jena, and D. Sahini, “Analysis of Mechanical Properties of Jute Epoxy Composite with Cenosphere Filler,” *Silicon*, vol. 11, pp. 659–671, 2019, doi: 10.1007/s12633-018-9941-x.
- [69] Z. Xing *et al.*, “Investigation of the Thermal Conductivity of Resin-Based Lightweight Composites Filled with Hollow Glass Microspheres,” *Polymers (Basel)*, vol. 12, no. 3, p. 518, Feb. 2020, doi: 10.3390/polym12030518.
- [70] A. Saygili and G. Baykal, “A new method for improving the thermal insulation properties of fly ash,” *Energy Build.*, vol. 43, no. 11, pp. 3236–3242, Nov. 2011, doi: 10.1016/j.enbuild.2011.08.024.
- [71] J. Bai, Y. Li, L. Ren, M. Mao, M. Zeng, and X. Zhao, “Thermal Insulation Monolith of Aluminum

- Tobermorite Nanosheets Prepared from Fly Ash,” *ACS Sustain. Chem. Eng.*, vol. 3, no. 11, pp. 2866–2873, Sep. 2015, doi: 10.1021/acssuschemeng.5b00808.
- [72] T. V Vakalova, T. A. Khabas, I. B. Revva, and I. A. Pavlova, “Heat-Insulating Ceramics which Have a Nanoporous Structure and are Made with the Use of Ash-Bearing Wastes from Power Plants,” *Refract. Ind. Ceram.*, vol. 55, no. 6, pp. 505–510, 2015, doi: 10.1007/s11148-015-9754-z.
- [73] W. Huo *et al.*, “Novel mullite ceramic foams with high porosity and strength using only fly ash hollow spheres as raw material,” *J. Eur. Ceram. Soc.*, vol. 38, no. 4, pp. 2035–2042, Apr. 2018, doi: 10.1016/j.jeurceramsoc.2017.11.002.
- [74] Z. Sun, C. Lu, J. Fan, and F. Yuan, “Porous silica ceramics with closed-cell structure prepared by inactive hollow spheres for heat insulation,” *J. Alloys Compd.*, vol. 662, pp. 157–164, Mar. 2016, doi: 10.1016/j.jallcom.2015.12.061.
- [75] Q. Wang, J. Chen, B. Gui, T. Zhai, and D. Yang, “Fabrication and Properties of Thermal Insulating Material using Hollow Glass Microspheres Bonded by Aluminum – Chrome – Phosphate and Tetraethyl Orthosilicate,” *Ceram. Int.*, vol. 42, no. 4, pp. 4886–4892, 2016, doi: 10.1016/j.ceramint.2015.12.003.
- [76] F. Motte, Q. Falcoz, E. Veron, and X. Py, “Compatibility tests between Solar Salt and thermal storage ceramics from inorganic industrial wastes,” *Appl. Energy*, vol. 155, pp. 14–22, 2015, doi: 10.1016/j.apenergy.2015.05.074.
- [77] L. N. Ngu, H. Wu, and D. K. Zhang, “Characterization of Ash Cenospheres in Fly Ash from Australian Power Stations,” *Energy and Fuels*, vol. 21, no. 6, pp. 3437–3445, 2007, doi: 10.1021/ef700340k.
- [78] F. J. Klug, S. Prochazka, and R. H. Doremus, “Alumina-Silica Phase Equilibria in the Mullite Region,” *J. Am. Ceram. Soc.*, vol. 70, no. 10, pp. 750–759, 1987.
- [79] V. S. Drozhzhin *et al.*, “Formation processes and main properties of hollow aluminosilicate microspheres in fly ash from thermal power stations,” *Solid Fuel Chem.*, vol. 42, no. 2, pp. 107–119, 2008, doi: 10.3103/S0361521908020110.
- [80] A. G. Fernández, B. Muñoz-Sánchez, J. Nieto-Maestre, and A. García-Romero, “High temperature corrosion behavior on molten nitrate salt-based nanofluids for CSP plants,” *Renew. Energy*, vol. 130, pp. 902–909, Jan. 2019, doi: 10.1016/j.renene.2018.07.018.
- [81] R. W. Bradshaw and S. H. Goods, “Corrosion Resistance of Stainless Steels During Thermal Cycling in Alkali Nitrate,” *Sandia Rep.*, no. SAND2001-8518, pp. 1–39, 2001.
- [82] A. Cox and D. J. Fray, “Mechanistic investigation into the electrolytic formation of iron from iron(III) oxide in molten sodium hydroxide,” *J. Appl. Electrochem.*, vol. 38, no. 10, pp. 1401–1407, 2008, doi: 10.1007/s10800-008-9579-2.
- [83] SQM, “SQM’s Thermo-Solar Salts: The Natural Solution for Thermal Storage and Heat Transfer in Your CSP Plant.” .
- [84] R. Gy, “Ion exchange for glass strengthening,” *Mater. Sci. Eng. B Solid-State Mater. Adv. Technol.*, vol. 149, no. 2, pp. 159–165, 2008, doi: 10.1016/j.mseb.2007.11.029.
- [85] T. Gross, “Chemical Strengthening of Glass,” in *Springer Handbook of Glass*, 2019, pp. 273–295.
- [86] Sinue Gomez, “A Look at the Chemical Strengthening Process: Alkali Aluminosilicate Glass Vs. Soda-Lime Glass,” 2011.

- [87] S. J. O'Connor, K. J. D. MacKenzie, M. E. Smith, and J. V. Hanna, "Ion exchange in the charge-balancing sites of aluminosilicate inorganic polymers," *J. Mater. Chem.*, vol. 20, no. 45, pp. 10234–10240, 2010, doi: 10.1039/c0jm01254h.
- [88] W. Höland and G. Beall, *Glass-Ceramic Technology*. 2019.
- [89] H. Ti Tien, "Ion exchange between alkali metal cations and sodium aluminosilicate gel at 276°, 298°, and 319°K," *J. Colloid Interface Sci.*, vol. 21, no. 1, pp. 94–98, 1966, doi: 10.1016/0095-8522(66)90083-3.
- [90] A. V. Petty, "A Study of the Strengthening of Glass by Ionic Diffusion," Georgia Institute of Technology, 1972.
- [91] J. S. Revathy, N. S. Chitra Priya, K. Sandhya, and D. N. Rajendran, "Structural and optical studies of cerium doped gadolinium oxide phosphor," *Bull. Mater. Sci.*, vol. 44, p. 13, 2021, doi: 10.1007/s12034-020-02299-wS.
- [92] R. Marin *et al.*, "Unexpected optical activity of cerium in $\text{Y}_2\text{O}_3:\text{Ce}^{3+}$, Yb^{3+} , Er^{3+} up and down-conversion system," *Dalt. Trans.*, vol. 42, p. 16837, 2013, doi: 10.1039/c3dt51297e.
- [93] R. Karmakar, S. K. Neogi, A. Banerjee, and S. Bandyopadhyay, "Structural, Morphological, Optical and Magnetic Property of Mn doped Ferromagnetic ZnO thin film," *Appl. Surf. Sci.*, vol. 263, pp. 671–677, 2012.
- [94] C. Suryanarayan and M. G. Norton, *X-Ray Diffraction: A Practical Approach*. New York, NY: Plenum Press, 1998.
- [95] R. D. Shannon, "Revised Effective Ionic Radii and Systematic Studies of Interatomic Distances in Halides and Chalcogenides," *Acta Crystallogr. Sect. A*, vol. 32, pp. 751–767, 1976.
- [96] Y.-K. Lee, Y. L. Peng, and M. Tomozawa, "IR reflection spectroscopy of a soda-lime glass surface during ion-exchange," *J. Non. Cryst. Solids*, vol. 222, pp. 125–130, 1997, doi: [https://doi.org/10.1016/S0022-3093\(97\)90104-6](https://doi.org/10.1016/S0022-3093(97)90104-6).
- [97] B. T. Poe, P. F. McMillan, C. A. Angell, and R. K. Sato, "Al and Si coordination in $\text{SiO}_2\text{-Al}_2\text{O}_3$ glasses and liquids: A study by NMR and IR spectroscopy and MD simulations," *Chem. Geol.*, vol. 96, no. 3–4, pp. 333–349, 1992, doi: 10.1016/0009-2541(92)90063-B.
- [98] H. Schneider, J. Schreuer, and B. Hildmann, "Structure and properties of mullite-A review," *J. Eur. Ceram. Soc.*, vol. 28, no. 2, pp. 329–344, 2008, doi: 10.1016/j.jeurceramsoc.2007.03.017.
- [99] H. Schneider, R. X. Fischer, and J. Schreuer, "Mullite: Crystal Structure and Related Properties," *J. Am. Ceram. Soc.*, vol. 98, no. 10, pp. 2948–2967, 2015, doi: 10.1111/jace.13817.
- [100] R. Balzer *et al.*, "Water in Alkali Aluminosilicate Glasses," *Front. Mater.*, vol. 7, no. May, 2020, doi: 10.3389/fmats.2020.00085.
- [101] M. Leśniak, J. Partyka, M. Gajek, and M. Sitarz, "FTIR and MAS NMR study of the zinc aluminosilicate ceramic glazes," *J. Mol. Struct.*, vol. 1171, pp. 17–24, 2018, doi: 10.1016/j.molstruc.2018.05.101.
- [102] G. Lucovsky *et al.*, "Local atomic structure of silicon suboxides (SiO_2 , $x < 2$)," *J. Non. Cryst. Solids*, vol. 75, no. 1–3, pp. 429–434, 1985, doi: 10.1016/0022-3093(85)90253-4.
- [103] N. Takamure, A. Kondyurin, and D. R. McKenzie, "Electric field assisted ion exchange of silver in soda-lime glass: A study of ion depletion layers and interactions with potassium," *J. Appl. Phys.*, vol. 125, no. 17, 2019, doi: 10.1063/1.5092545.

- [104] H. Aguiar, J. Serra, P. González, and B. León, "Structural study of sol-gel silicate glasses by IR and Raman spectroscopies," *J. Non. Cryst. Solids*, vol. 355, no. 8, pp. 475–480, 2009, doi: 10.1016/j.jnoncrysol.2009.01.010.
- [105] M. Todea, R. V. F. Turcu, B. Frentiu, and S. Simon, "FTIR and NMR evidence of aluminosilicate microspheres bioactivity tested in simulated body fluid," *J. Non. Cryst. Solids*, vol. 432, pp. 413–419, 2016, doi: 10.1016/j.jnoncrysol.2015.10.039.
- [106] N. S. Jacobson and K. N. Lee, "Corrosion of Mullite by Molten Salts," *J. Am. Ceram. Soc.*, vol. 79, no. 8, pp. 2161–2167, 1996.
- [107] S. Komarneni, H. Schneider, and K. Okada, "Mullite Synthesis and Processing," in *Mullite*, 2005, pp. 251–348.
- [108] K. Sharma, M. N. Deo, and G. P. Kothiyal, "Effect of iron oxide addition on structural properties of calcium silico phosphate glass/glass-ceramics," *J. Non. Cryst. Solids*, vol. 358, no. 16, pp. 1886–1891, 2012, doi: 10.1016/j.jnoncrysol.2012.05.034.
- [109] P. Stoch, W. Szczerba, W. Bodnar, M. Ciecinska, A. Stoch, and E. Burkel, "Structural properties of iron-phosphate glasses: Spectroscopic studies and ab initio simulations," *Physical Chemistry Chemical Physics*, vol. 16, no. 37, pp. 19917–19927, 2014, doi: 10.1039/c4cp03113j.
- [110] S. Ibrahim, M. M. Gomaa, and H. Darwish, "Influence of Fe_2O_3 on the physical, structural and electrical properties of sodium lead borate glasses," *J. Adv. Ceram.*, vol. 3, no. 2, pp. 155–164, 2014, doi: 10.1007/s40145-014-0107-z.